Measurement and prediction of the transformation strain that controls ductility and toughness in advanced steels

Maresca, Francesco; Polatidis, Efthymios; Smid, Miroslav; Van Swygenhoven, Helena; Curtin, William

Published in:
Acta Materialia

DOI:
10.1016/j.actamat.2020.08.028
https://doi.org/10.1016/j.actamat.2020.08.028

Acta Materialia 200 (2020) 246–255

Contents lists available at ScienceDirect

Acta Materialia

journal homepage: www.elsevier.com/locate/actamat

Full length article

Measurement and prediction of the transformation strain that controls ductility and toughness in advanced steels

Francesco Maresca[a,b,*], Efthymios Polatidis[c], Miroslav Šmíd[c], Helena Van Swygenhoven[c,d], William A. Curtin[b]

[a] Engineering and Technology Institute Groningen, Faculty of Science and Engineering, University of Groningen, 9747 AG, Netherlands
[b] Laboratory for Multiscale Mechanics Modeling, Institute of Mechanical Engineering, École Polytechnique Fédérale de Lausanne, Lausanne CH-1015, Switzerland
[c] Photons for Engineering and Manufacturing, Photon Science Division, Paul Scherrer Institute, Villingen-PSI CH-5232, Switzerland
[d] Neutrons and X-rays for Mechanics of Materials, Institute of Materials, École Polytechnique Fédérale de Lausanne, Lausanne CH-1015, Switzerland

ARTICLE INFO

Article history:
Received 15 January 2020
Revised 20 July 2020
Accepted 10 August 2020
Available online 27 August 2020

ABSTRACT

New-generation multi-phase martensitic steels derive their high strength from the body-centered cubic (BCC) phase and high toughness from transformation of the metastable face-centered cubic (FCC) austenite that transforms into martensite upon loading. In spite of its critical importance, the in-situ transformation strain (or "shape deformation" tensor), which controls ductility and toughness, has never been measured in any alloy where the BCC lath martensite forms and has never been connected to underlying material properties. Here, we measure the in-situ transformation strain in a classic Fe-Ni-Mn alloy using high-resolution digital image correlation (HR-DIC). The experimentally obtained results can only be interpreted using a recent theory of lath martensite crystallography. The predicted in-situ transformation strain agrees with the measurements, simultaneously demonstrating the method and validating the theory. Theory then predicts that increasing the FCC to BCC lattice parameter ratio substantially increases the in-situ transformation strain magnitude. This new correlation is demonstrated using data on existing steels. These results thus establish a new additional basic design principle for ductile and tough alloys: control of the lattice parameter ratio by alloying. This provides a new path for development of even tougher advanced high-strength steels.

1. Introduction

The urgent need for energy efficiency and reduced emissions is driving the development of new lightweight, high strength, high-toughness, affordable structural materials. Among the most promising are multiphase martensitic steels (such as those investigated in [1]) that derive high strength from the body centered cubic (BCC) "lath martensite" phase [2–4] and high toughness from transformation of the metastable face-centered (FCC) austenite that transforms into martensite upon loading. The achievable ductility in martensitic steels (such as those studied in [1], but also [5–7]) is limited by the transformation strain and volume fraction of the transformable austenite. The in-situ transformation strain is a tensorial quantity and is also called the shape deformation, and is usually indicated in the martensite crystallography literature [8,9] as $\mathbf{P}^{(1)}$ and in much of the micromechanics modelling literature [10] as $\mathbf{F}_{tr}$. This transformation strain is accommodated by plasticity and thus dissipates energy as well as provides the strain that increases ductility [11,12]. This connection between micromechanical behaviour and macroscopic response has been the subject of a number of investigations, e.g. [13–17] but see also [10] for a general review.

In spite of its critical role for performance, the full 3D in-situ transformation strain has never been measured directly in any alloy where lath martensite is formed, even for standard alloys such as Fe-C [3,18] and Fe-Ni-Mn [19–21]. The challenges include achieving sufficient resolution of fine sub-micron regions within the material, determining the full 3D transformation strain when only in-plane components can be measured, and isolating transformation from other deformation mechanisms such as crystallographic slip [22] or twinning [7]. The measurement is thus not

* Corresponding author at: Engineering and Technology Institute Groningen, Faculty of Science and Engineering, University of Groningen, 9747 AG, Netherlands.
E-mail address: f.maresca@rug.nl (F. Maresca).

https://doi.org/10.1016/j.actamat.2020.08.028

possible without an accompanying predictive theoretical framework for the transformation.

Here, we determine the full in-situ transformation strain tensor for the classic Fe-20.2%Ni-5.4%Mn alloy using an adroit combination of state of the art high-resolution digital image correlation [23], electron backscattered diffraction, scanning electron microscopy, neutron diffraction, and theory. The experimental results allow to measure only the in-plane strain components, and hence the full in-situ transformation strain tensor can only be determined using recent theory [24]. The predicted in-situ transformation strain agrees with the measurements, simultaneously demonstrating the method and further validating the crystallographic theory.

Theory then predicts that increasing the FCC to BCC lattice parameter ratio substantially increases the in-situ transformation strain magnitude, which relates to enhanced ductility. This new correlation is demonstrated using data on existing steels, and is not simply related to the lattice parameter ratio entering the Bain strain as in many shape-memory alloys (e.g. [25]). These results thus establish a new additional basic design principle for ductile and tough steel alloys: control of the lattice parameter ratio, and hence the transformation strain, by alloying. This provides a new path for guiding development of even tougher advanced high-strength steels.

The paper is organized as follows. Section 2 presents the details of the experimental procedures adopted to process, characterize and test mechanically the Fe-Ni-Mn alloy. Section 3 summarizes the main features of the theory proposed in [24] and the details of the calculations using experiments as input. Section 4 shows the main results of the paper, including validation of the in-plane strain components and the theory predictions of the full 3D transformation strain. We discuss our findings in Section 5, where the new correlation between lattice parameter ratio and in-situ transformation strain is shown based on published data on alloys where the FCC to BCC transformation occurs.

2. Experimental

2.1. Materials

A Fe-20.2Ni-5.4Mn (wt.%) alloy was prepared in molten state from pure granules of the alloying elements (i.e. Fe: 99.98%, Ni: 99.99%, Mn: 99.9%) in an induction furnace and cast in a cylindrical ceramic mould of 25 mm diameter. The ingot was then encapsulated in a quartz tube and homogenized at 1473 K for 3.6 ks followed by water quenching (by breaking the tube). The obtained cylindrical ingot was sliced into buttons of ~ 1 mm thickness and exposed to 193 K for 8 h to thermally induce martensite. The buttons were ground using 360, 600, 1200 and 2500 grit paper down to 0.3 mm thickness and dogbone samples were cut by picosecond laser ablation at the Swiss Federal Laboratories for Materials Science and Technology (EMPA).

2.2. Neutron diffraction and TEM measurements

Key to the analysis are the FCC and BCC lattice parameters; only with the correct lattice parameter ratio can theory and experiment be brought together [24]. Neutron diffraction yields the lattice parameter of austenite $a_{fcc} = 3.58167 \pm 3.8\ 10^{-5}$ Å while transmission electron microscopy (TEM) yields the BCC lattice parameter $a_{bcc} = 2.9058 \pm 0.0159$ Å. The neutron diffraction measurement of the lattice parameter of austenite was undertaken at the POLDI instrument at SINQ [26,27]. Fitting of the diffraction spectrum was performed using the built-in Pawley fit routine in Mantid [28]. Since the alloy contains limited volume fraction of martensite, it was not possible to measure its lattice parameter by neutron diffraction. Thus, selected area electron diffraction was performed using a TEM JEOL JEM 2010 on a TEM lamella prepared by focused ion beam technique. Multiple diffraction patterns of several prominent zone axes have been used to obtain statistically reliable lattice constant values. Since conventional TEM is not ideal for measuring, with high precision, the lattice parameter, a correction factor was applied to the measured lattice parameters derived from a Si standard, since the Si lattice parameter is known with high accuracy from the literature. We have found that the Si lattice parameter, measured with ± 0.01 Å standard deviation in TEM, must be multiplied by a factor of 1.0426 to match the established, literature lattice parameter. We have thus used this scaling factor to multiply the TEM measurements of both the austenite and the martensite lattice parameter. The corrected TEM measurement of the FCC lattice parameter is $a_{fcc} = 3.586 \pm 0.01$ Å, which is in very good agreement with the neutron diffraction measurement, since this falls within the TEM measurement accuracy. By using the ratio between the neutron diffraction FCC lattice parameter and the TEM one before applying any correction, we obtain the correction factor 1.0412 which is close within ~ 0.1% accuracy to the one calculated based on the Si lattice parameter. We therefore conclude that the TEM measurements using multiple reflections and different zone axes, and including the correction based on Si lattice parameter, yield accurate values for the FCC and the BCC lattice parameters.

2.3. Pre-straining

The dogbone sample was pre-strained up to 33% strain using the “meso-biaxial machine” (maximal load 1000 N) described in [29]. The pre-straining was performed to provide nucleation sites for stress-induced martensite and to expand the existing, thermally-induced martensite. The pre-strained sample was then ground down to 90 µm, so that it could be deformed with the “mini-biaxial machine” [30], which fits in SEM (maximal load 40 N). Thus, the microstructure observed at the start of HRDIC measurements is representative of the bulk material, rather than resulting from surface effects.

2.4. EBSD characterization

The dogbone surface was finished by electropolishing with a solution of ethanol, glycerol and $HClO_4$ (volume ratio 16:3:1) at 42 Volts with a medium stirring speed of the electrolyte for 13s to obtain a surface quality suitable for Electron Backscatter Diffraction (EBSD) investigation. Prior to the *in-situ* deformation test, EBSD investigation was undertaken to find regions where martensite had formed. A FEG SEM Zeiss ULTRA 55 with an EDAX Hikari Camera operating at 20kV in high current mode and with 120 µm aperture was used for EBSD characterization. The EBSD raw data were post-processed using the EDAX OIM Analysis 7.3 software.

2.5. Digital image correlation

The fine gold speckle pattern for the High Resolution Digital Image Correlation (HRDIC) was obtained by the remodeling process of a thin gold layer sputtered on the surface of the polished sample [23], under a current of 20 mA for only 30 s at a distance of about 50 mm from the gold target. The mini-biaxial machine was installed inside the chamber of the FEG SEM Zeiss ULTRA 55 microscope. The deformation tests were performed in displacement control with a displacement rate of 0.2 µm/s. SEM imaging was undertaken at an acceleration voltage of 3 keV with a 30 µm aperture opening. The images were acquired with an in-lens detector at a working distance (WD) of 6.7 mm in order to minimize the topographic contrast by gathering low energy electrons, providing a good signal/noise ratio. The 90 µm dogbone sample was loaded uniaxially in the elastic regime until 275 MPa (~ 0.1% global strain)

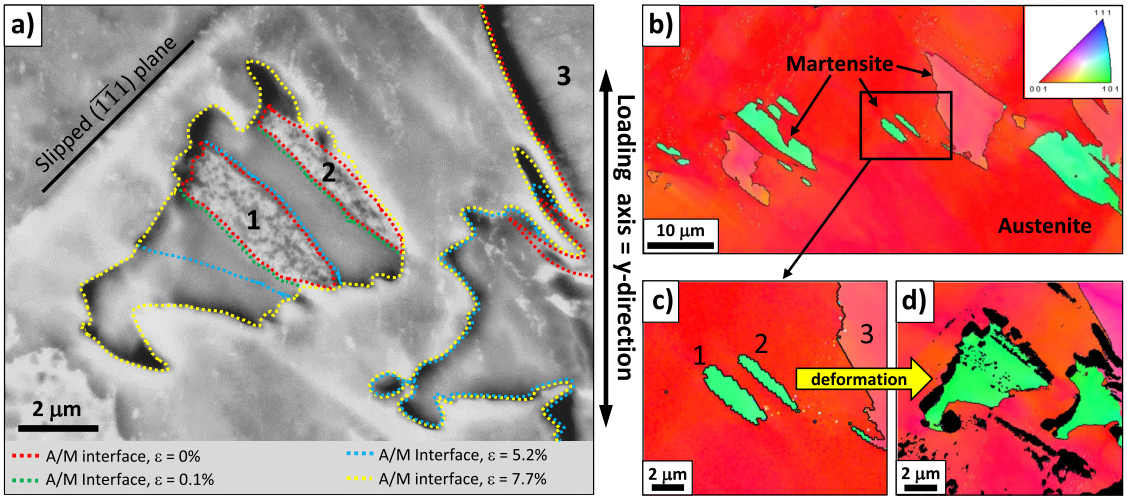

Fig. 1. SEM and EBSD measurements of austenite-martensite phase transformation. **a** SEM image after the completed test (strained to 7.7% and then unloaded), showing the final shape of the grown martensite grain (yellow dashed lines). The martensite grain grows from two individual martensite islands that pre-exist at the start of the *in-situ* deformation test (outlined with the red dashed lines). The subsequent boundaries are derived by the evolution of the DIC strain (cf. Fig. 2) during loading and are indicated in green color (at global 0.1% applied strain), blue (at global 5.2% strain) and yellow (at global 7.7% strain). **b** Electron-Backscattered Diffraction (EBSD) and Inverse Pole Figure (IPF) maps (out of plane) showing the initial martensite particles. **c** Magnified section of the EBSD inverse IPF map prior to the *in-situ* deformation, showing the initial martensite islands 1, 2 and 3. **d** EBSD inverse IPF map after the *in-situ* test showing the large martensite grain grown in place of islands 1 and 2, as well as the growth of a spike from island 3. (For interpretation of the references to color in this figure legend, the reader is referred to the web version of this article.)

and a first HR-DIC was taken. Then the sample was further loaded to a total strain of 5.2% and 7.7%, calculated by the displacement of the grips with respect to the length of the gauge section, which is 3 mm. The HRDIC analysis was undertaken with the Ncorr code [31], using a subset radius of 15 pixels, 0 subset spacing and a strain radius of 3 pixels. After the HRDIC investigation, the gold particles were removed from the surface of the samples using an etching solution of HCl, H_2O, and HNO_3 (volume ratio 11:8:1) so that *post-mortem* EBSD and SEM investigations could be undertaken. It was seen that the etchant preferably attacked martensite, more than austenite, resulting in pronounced topographic features. The fact that the martensite is still found after etching confirms that phase transformation is not occuring only at the very surface, but also in the depth of the region between the two pre-existing martensite islands.

2.6. Initial microstructure

The Fe-20.2Ni-5.4 Mn (wt%) alloy has large FCC austenite grains and BCC lath martensite [20]. A region with two elongated martensite islands was identified as an ideal site to perform deformation measurements using *in-situ* High Resolution Digital Image Correlation (HR-DIC) in a Scanning Electron Microscope (SEM), Fig. 1. Before testing, the crystallographic orientations of the austenite and martensite were measured (Fig. 1b) by electron backscatter diffraction (EBSD). In this region, the relatively straight martensite boundaries reduce possible morphological effects on the local strains that drive the transformation. The austenite slip systems (associated with transformation [17]), are in a favorable orientation with respect to the loading axis. The specific austenite orientation in this region is such that deformation by crystallographic slip along the slip system with highest Schmid Factor (SF) affects only one of the three in-plane Green-Lagrange strain components. Meeting all of these requirement is a formidable task but is essential for proper measurement and comparison with theory.

3. Theory

To determine the full 3D transformation strain, we use our recent, *parameter-free* theory of martensite crystallography [24]. Note, that this theory has the same mathematical structure as the double-shear versions of the *phenomenological* theory of martensite crystallography (PTMC), such as [8,37,38] that involve two lattice invariant deformations due to crystallographic slip. However, the theory in [24] is *predictive* because, unlike the previous PTMC versions, the lattice invariant deformations are known, based on the detailed atomic-scale analysis of the austenite/martensite interface. The in-situ transformation is described by the deformation tensor $\mathbf{P}^{(1)}$, also called the shape deformation, which has the form of an invariant-plane strain deformation [24]

$$\mathbf{P}^{(1)} = \mathbf{I} + m^{(1)}\mathbf{s}^{(1)} \otimes \mathbf{n}^{(1)} \tag{1}$$

where $\mathbf{I}$ is the identity tensor, $m^{(1)}$ is the transformation strain *magnitude*, $\mathbf{s}^{(1)}$ is the transformation *direction* and $\mathbf{n}^{(1)}$ is the FCC-BCC interface plane or *habit plane* normal. The shape deformation is determined by (i) the well-known Bain tensor $\mathbf{B}$ [32] that transforms isolated FCC to isolated BCC and depends only on the FCC/BCC lattice parameter ratio r and (ii) the lattice-invariant shear deformations $\mathbf{P}^{(2)}$ and $\mathbf{P}^{(3)}$ that are created by the two sets of dislocations formed at the interface that were established through an atomistic study of the FCC/BCC interface [24]. The shear $\mathbf{P}^{(3)}$ is associated with the $a_{fcc}/2[\bar{1}01]$ interface screw dislocations, while $\mathbf{P}^{(2)}$ is due to $a_{bcc}/2[1\bar{1}1]$ near-screw interface dislocations. Furthermore, $\mathbf{P}^{(2)}$ is associated with the orientation relationship φ at the interface and $\mathbf{P}^{(3)}$ is related to the density of steps along the interface. The interface steps and the $a_{bcc}/2[1\bar{1}1]$ near-screw interface dislocations agree with multiple TEM and HRTEM evidences [20,21,33], as well as with Molecular Dynamics (MD) simulations of the interface structure [24]. To the best of our knowledge, no other theories for lath martensite agree with experiments and MD simulations in all these aspects.

The shape deformation is then computed as

$$\mathbf{P}^{(1)} = \mathbf{R}_{\Delta} \cdot \mathbf{R} \cdot \mathbf{B} \cdot \mathbf{P}^{(3)} \cdot \mathbf{P}^{(2)} \tag{2}$$

where $\mathbf{R}_{\Delta}$ is a far-field micro-rotation and $\mathbf{R}$ is the rotation associated with φ. The step density contained in $\mathbf{P}^{(3)}$ is determined by requiring that $\mathbf{P}^{(1)}$ have the form of Eq. (1). This is equivalent to satisfying the compatibility condition, for which the intermediate eigenvalue of $\mathbf{C} = \left[\mathbf{P}^{(1)}\right]^{T} \cdot \mathbf{P}^{(1)}$ equals 1. The experimentally-

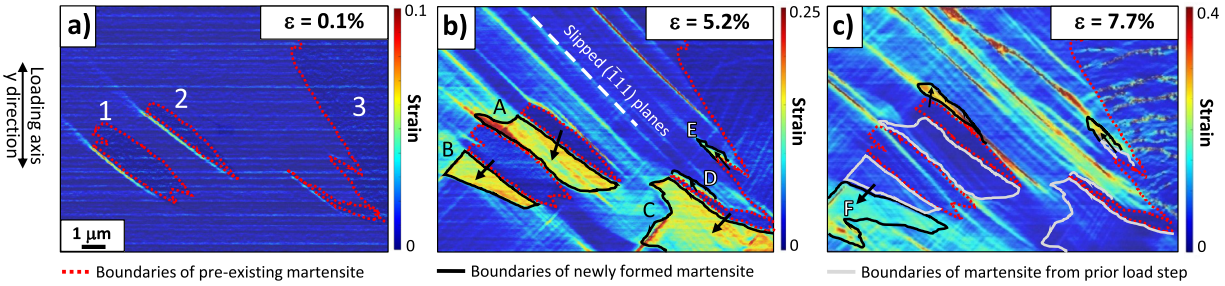

Fig. 2. HR-DIC measurements of austenite-martensite phase transformation. HR-DIC maps showing the propagation of the martensite boundaries as apparent by the evolution of the strain fields, associated with the transformation, **a** during elastic loading, i.e. at 0.1% global strain (275 MPa), **b** at 5.2% global strain (415 MPa) and **c** upon loading from 5.2% to 7.7% global strain (from 415 MPa to 435 MPa). Dashed colored lines indicate the martensite boundaries at the different strain levels using colors that provide contrast against the strain background. Black arrows indicate the growth direction of the new martensite. By convoluting the boundaries of the initial martensite and the newly formed martensite until 7.7% global strain, the final shape of the martensite island shown in Fig. 1 can be outlined. (For interpretation of the references to color in this figure legend, the reader is referred to the web version of this article.)

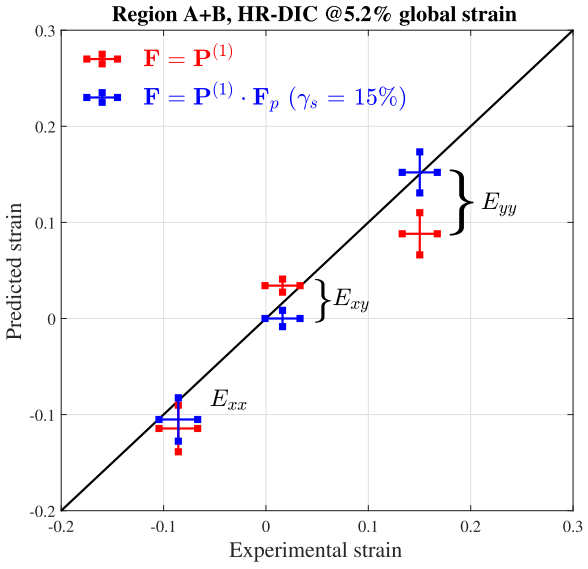

Fig. 3. Predictive theory of martensite transformation *vs* experiments in Fe20Ni5Mn. Theory predictions of the *in-situ* transformation strain (shape deformation) versus experimentally-measured in-plane strains (red symbols with error bars), at 5.2% global strain. The error bars indicate the standard deviation of the strain measurements within the region where the phase transformation occurs. The strain component E_{yy} is underpredicted because the experimental strains include crystallographic slip. Including slip along the fcc slip system with the largest Schmid factor brings theory and experiment into full agreement, with slip contributing only slightly to the strain components E_{xx} and E_{xy} while rectifying the difference in E_{yy}. (For interpretation of the references to color in this figure legend, the reader is referred to the web version of this article.)

measured strain is the Green-Lagrange strain tensor that is computed from the theory as $\mathbf{E} = \frac{1}{2}[\mathbf{C} - \mathbf{I}]$.

In order to apply the crystallographic theory using experimental input, only the Fe-20.2Ni-5.4Mn alloy lattice parameter ratio $a_{\text{fcc}}/a_{\text{bcc}} = 1.233$ and the average orientation relationship $\varphi = 3.7^\circ$ are used. Theory predictions are also performed at the lower and upper bounds of the lattice parameter ratio ($r = 1.226 - 1.239$), that result from the standard deviation associated with the measurements of the lattice parameters. As detailed in the Appendix A, the determination of $\mathbf{P}^{(1)}$ is done here by considering experimental austenite crystal coordinates and the *in-situ* measurement of crystallographic martensite variants (relative orientation of martensite with respect to austenite). To this end (but see Appendix A for details), the Euler angles of multiple measurement points in the austenite are considered in order to account for the effect of small orientation fluctuations on the theoretical predictions. Furthermore, the martensite orientation is also considered in order to determine the specific crystallographic variant that has formed experimentally. Thus, the calculation of $\mathbf{P}^{(1)}$ is performed for this experimentally measured variant, and the predicted $\mathbf{P}^{(1)}$, which is expressed in the austenite crystallographic basis, is then written in the specimen coordinates ($\mathbf{P}^{(1)*}$) by using the experimental austenite Euler angles, in order to be able to compare the theory predictions with the experimental measurements. From $\mathbf{P}^{(1)*}$, the in-plane components of the Green-Lagrange strain are then determined by using the same definition as the one reported in the Ncorr manual [31], which is used for the HR-DIC experimental results.

4. Results

4.1. Mechanical testing

HR-DIC in the global "elastic" loading regime showed early growth of martensite along the pre-existing boundaries (Fig. 2a). This is consistent with the interface propagation mechanism reported in our recent molecular dynamics simulations [24]. At 5.2% strain (Fig. 2b), the entire austenitic region between the two pre-existing martensite islands, and a region adjacent to the lower martensite island, have transformed to martensite. The newly-grown martensite grows crystallographically matched (same variant) with the pre-existing bulk martensite and so the in-situ transformation strain is not affected by the surface measurement. HR-DIC measurements between 0 and 5.2% strain yield the spatial distribution of in-plane Green-Lagrange strains E_{xx}, E_{yy} (Fig. 2) and E_{xy}. Fig. 6 in the Appendix B shows the strain maps related to the three in-plane Green-Lagrange strain components measured at 5.2% strain. The HR-DIC strain maps show relatively uniform deformation in the transformed regions but with some more-localized deformation along the slip plane with maximum Schmid factor that is attributed to crystallographic slip (see below). There is significant plasticity on either ends of all the new martensite: this is the TRIP effect that gives the energy dissipation. Furthermore, slip bands on the upper portion of the HR-DIC map at 5.2% strain, far from the martensite, are associated with typical $E_{yy} \simeq 6\%$ strain component, which corresponds to $\simeq 15\%$ shear strain along the slip system having the highest Schmid factor.

Upon further loading, the martensite grows as shown in Fig. 2c, while slip bands become more apparent. By the end of the test, the two initial martensite islands coalesce and become one single particle, as shown in the "post-mortem" EBSD in Fig. 1d. The SEM

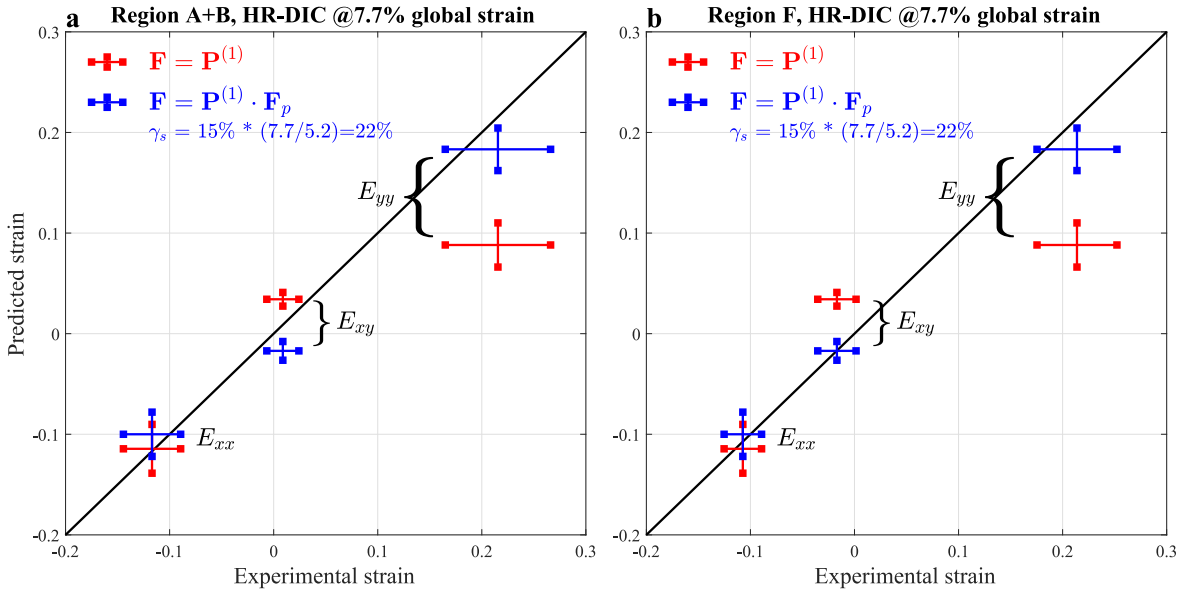

Fig. 4. Theory predictions *vs* experiments in Fe20Ni5Mn, between 0 and 7.7% global strain. Theory predictions of the *in-situ* transformation strain (shape deformation) versus experimentally-measured in-plane strains (red symbols with error bars). The error bars indicate the standard deviation of the strain measurements within the region where the phase transformation occurs. Including slip along the fcc slip system with the largest Schmid factor brings theory and experiment into full agreement. The total slip is increased proportionally from the value assumed at 5.2%, and hence is not adjusted to fit the data. **a** Theory predictions *vs* experimental measurements from the regions A and B, that are adjacent to the pre-existing martensite islands 1 and 2. **b** Theory predictions *vs* experimental measurements from the region F, which corresponds to a new, large martensite islands that forms at 7.7% strain (bottom-left corner of Fig. 2c). (For interpretation of the references to color in this figure legend, the reader is referred to the web version of this article.)

micrograph in Fig. 1a shows the grown martensite after the in-situ deformation test.

4.2. *Theory predictions* vs *experiments*

The full 3D transformation strain for the Fe-20.2Ni-5.4 Mn (wt%) is predicted to be

$$\mathbf{P}^{(1)} = \mathbf{I} + 0.3962 \cdot [-0.8265, 0.374, 0.4207]_{\text{fcc}} \otimes (0.3799, 0.8227, 0.4229)_{\text{fcc}}$$

as written for the crystallographic variant $(111)_{\text{fcc}} \| (011)_{\text{bcc}}$ and orientation $\varphi = 3.7^\circ$ between $[\bar{1}01]_{\text{fcc}}$ and $[\bar{1}\bar{1}1]_{\text{bcc}}$. The magnitude of the transformation strain is thus 39.62%. By considering the standard deviation in the lattice parameter measurements, the magnitude of the *in-situ* transformation strain ranges between 36% and 44%. The theory has no free parameters and so is a true prediction.

The theory prediction can be compared to the HR-DIC measurements. Fig. 3 shows the predicted and measured values for the 3 in-plane strain components E_{xx}, E_{xy}, and E_{yy}, where the measurements are taken between 0 and 5.2% global strain. Two components, E_{xx} and E_{xy}, are predicted within the measurement accuracy. E_{yy} differs due to plastic slip, as discussed next. The error bars in the predictions are due to the variation in the lattice parameter ratio and small variations in the austenite orientation prior to the transformation. The error bars related to the experiments represent the standard deviation with respect to the average strain measurement in the region where transformation occurs. Here, the average is computed only in the regions A and B, which transform next to martensite islands 1 and 2 (see Fig. 2), since morphological effects are lower in these regions due to the straight boundaries of the pre-existing martensite and only one slip system is observed to activate in these regions. Comparable strain components are measured also for the other regions that transform (see also Appendix B), and hence the measurement is representative of the transformation strain of multiple regions.

The predicted magnitude of E_{yy} is smaller than experiments precisely because the experiments include an additional plastic slip strain in exactly this direction. This slip is clearly shown in the experiments by the slip traces in Fig. 2b. The experiment measures the total strain, which includes the strain due to the plastic slip, which is separate from the in-situ transformation strain. It is not possible to quantitatively separate the slip and transformation contributions because they occur simultaneously [22]. However, plastic slip can be introduced into the theory by including an average shear deformation $\mathbf{F}_p$ due to the crystallographic slip that must be of the form

$$\mathbf{F}_p = \mathbf{I} + \gamma_s \mathbf{s} \otimes \mathbf{n}. \tag{3}$$

Here, γ_s is the magnitude of the crystallographic shear slip in direction $\mathbf{s}$ on slip plane with normal $\mathbf{n}$. We consider the slip system with highest Schmid factor, which is also the slip system observed to be active in the experiment. The total deformation is then predicted to be

$$\mathbf{F} = \mathbf{P}^{(1)} \cdot \mathbf{F}_p. \tag{4}$$

The total strain $\mathbf{E}$ is then obtained from $\mathbf{F}$ using $\mathbf{C} = \mathbf{F}^T \cdot \mathbf{F}$. Although the plastic strain magnitude is unknown, the extended theory matches experiments very well for an average plastic shear of $\gamma_s = 15\%$, as shown in Fig. 3. This average plastic shear strain increases the prediction of the total strain E_{yy} by 0.06, but does not affect either E_{xx} or E_{xy}. The agreement between theory and experiment for E_{xx} and E_{xy} is thus preserved upon introduction of the additional plastic slip. The additional average E_{yy} strain of 0.06 is roughly consistent with the localized slip traces around the transformed martensite that can reach typical local values as high as ~ 0.25. We reiterate that E_{xx} and E_{xy} are accurately predicted by the theory independent of any additional plastic slip, and a realistic plastic slip magnitude in the direction of the observed plastic slip brings E_{yy} into agreement with experiments as well.

To validate the theory further, Fig. 4a compares the theoretical predictions of E_{xx}, E_{xy} and E_{yy} to the HR-DIC measurements taken between 0 and 7.7% global strain for the regions A and B that are next to the martensite islands 1 and 2, where the morphological effects are lower (see Appendix B for the HR-DIC mea-

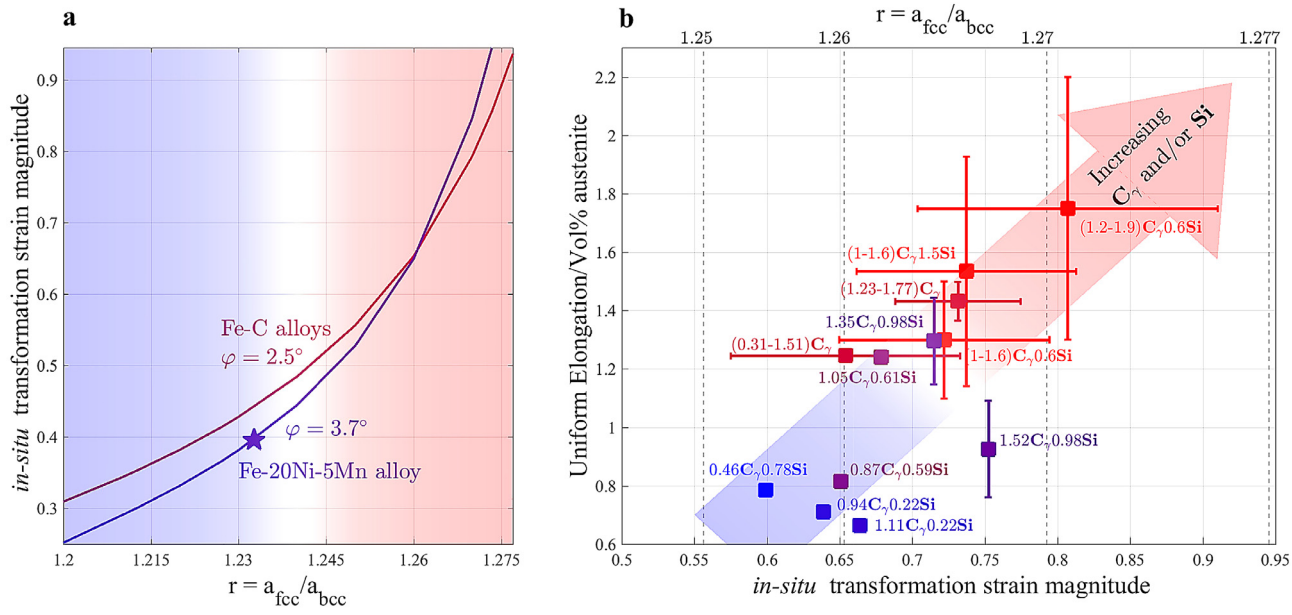

Fig. 5. *in-situ* transformation strain magnitude controlled by lattice parameter ratio. a Theory predictions of the *in-situ* transformation strain magnitude versus lattice parameter ratio $r = a_{fcc}/a_{bcc}$, for typical average orientation relationships φ relevant for Fe-Ni-Mn [20] and Fe-C [49] alloys. Larger lattice parameter ratios are predicted to significantly increase the *in-situ* transformation strain, which determines alloy toughness and ductility. **b** Experimentally-measured uniform elongation per austenite volume fraction, a measure of ductility and toughness, versus the *in-situ* transformation strain (bottom scale) and lattice parameter ratio (top scale), for a wide range of Fe-C "TRIP-aided" alloys investigated in [39–44]. $\mathbf{C}_\gamma$ is the reported carbon content in the austenite phase. Ductility is significantly enhanced by increasing the lattice parameter ratio, achieved in these alloys by increasing C or Si content, demonstrating the key role of lattice parameter ratio as an alloy design parameter for achieving high toughness.

surements between 0 and 7.7% global strain). Without any correction for plastic slip, the component E_{xx} is again predicted within the measurement accuracy while E_{xy} and E_{yy} differ due to plastic slip. The meaning of the error bars is the same as in Fig. 3. We then include plastic slip into the theory using Eqs. (3) and (4) and the slip system observed to be active in the experiment. The magnitude of the crystallographic slip γ_s is not fit, but is computed by assuming that the global slip and local slip are proportional. Thus, the local plastic slip at 7.7% global strain is taken to be $\gamma_s = 0.15 * (7.7/5.2) = 0.22$. The predicted strain components are shown in Fig. 4a and agree well with the experiments. This further confirms that the measured in-plane strain components have contributions from both the intrinsic *in-situ* transformation strain $\mathbf{P}^{(1)}$, which is predicted by the crystallographic theory, and the extrinsic plastic slip on the active slip system.

Finally, Fig. 4b compares the theory predictions to the HR-DIC measurements from the new large martensite island that forms at 7.7% global strain (region F, see bottom-left corner of Fig. 2c). Despite the more complex morphology, the theory predictions including both the transformation strain and the same amount of crystallographic slip on the active slip system are again in good agreement with experiments.

In total, the theory accurately predicts the experimental in-plane strain components E_{xx}, E_{xy} and E_{yy} in three different regions of transformation and at two different global strain levels when the crystallographic theory is extended to include the observed active plastic slip.

5. Discussion

The only prior estimate of the in-situ transformation strain magnitude in this class of steels is that from Wakasa and Wayman [36], who estimated ~ 30% for the Fe-20.2Ni-5.4 Mn alloy based on surface relief measurements using scratch displacements in SEM and interference fringes in an optical microscope. The in-situ transformation direction could not be determined. Sandvik and Wayman [8] attempted shortly after to perform theory predictions, based on careful crystallographic analysis of the interface. However, without knowing the interface defect structure and hence the combination of lattice invariant shear revealed in [24], and by using the incorrect lattice parameter ratio (1.249, which is based on measurements on a different alloy, namely Fe-31Ni), they predicted a transformation strain magnitude equal to 0.96, which according to their own words "is still much larger" than estimated in [36]. Our results here are thus the first accurate determination of the full in-situ transformation strain in any austenitic-martensitic steel where lath martensite forms, achieved only by a combination of state-of-the-art experiment and recent theory.

The agreement here is a strong experimental validation of the crystallographic theory of phase transformation. The theory can therefore now be applied with confidence to predict the transformation strain in transforming alloys where the FCC to BCC transformation occurs as a function only of the lattice parameter ratio r. Fig. 5 shows the predictions of the in-situ transformation strain versus r for values of φ typical of Fe-Ni-Mn and Fe-C. Very high strains, and hence high ductility and toughness, is predicted for increased FCC lattice parameter a_{fcc} and/or decreased BCC lattice parameter a_{bcc}.

It is useful to note that although the underlying ex-situ Bain strain depends on r, that dependence is weak and negligible in terms of contributing to the transformation strain. It is the in-situ crystallography of the transformation process that creates a huge magnification of the in-situ transformation strain as compared to the Bain strain $\mathbf{B}$. Specifically, the maximum shear strain associated with the strain $\mathbf{B} - \mathbf{I}$ is $\frac{1}{2r}\left(\sqrt{2} - 1\right)$, which falls in the range 0.162 - 0.173 for r in the range 1.2 - 1.275. The dependence of the Bain strain on r is thus extremely weak for realistic ranges of r, the trend with r is even opposite to that found for the in-situ transformation strain, and it is much smaller than the true in-situ transformation strain. Furthermore, the importance of the lattice invariant shears $\mathbf{P}^{(2)}$ and $\mathbf{P}^{(3)}$ for the total shape deformation can be observed by computing the shape deformation due only to the Bain strain, $\mathbf{P}^{(1)} = \mathbf{R} \cdot \mathbf{B}$, from which the in-plane strain compo-

nents corresponding to the experiments are $E_{xx} = 0.16$, $E_{xy} = -0.02$ and $E_{yy} = -0.17$. These strains are both quantitatively and qualitatively wrong. Thus, the Bain strain is just a part of the total in-situ transformation strain. This is fully consistent with the well-established understanding of the theory of martensite crystallography in steels [9].

The key role of r (beyond the basic Bain strain) does not emerge from any previous theories [8,37,38], and its importance for lath martensite in steels has never been appreciated prior to [24]. For instance, to explain the transformation strain in Fe-20Ni-5Mn, Ref. [8] actually used the value $r = 1.249$ relevant for the Fe-31Ni alloy. Use of the Fe-31Ni value in our theory leads to no agreement at all with experiment for E_{xx} and E_{xy} in Fe-20Ni-5Mn. In Ref. [24], we also used the incorrect value of r given in Ref. [8], and hence the predicted transformation strain in our previous paper is incorrect but there was no experimental value for comparison at that time and so the error in Ref. [24] is of no consequence.

Lattice parameter variations can be achieved by alloying, and so this range can be explored. The present analysis introduces a new critical variable r through which the ultimate properties of ductility and toughness can be enhanced. This new insight of the theory enables us to re-evaluate existing advanced steels in a new context, which then further supports our new proposed alloy design strategy based on control of r. Fig. 5b shows the correlation between alloy ductility, represented as uniform elongation per volume fraction of austenite, versus measured lattice parameter ratio and versus the predicted *in-situ* transformation strain. The data encompasses all work we could find that provided data on alloy composition, austenite volume fraction, lattice parameters, and measured mechanical properties; the error bars indicate the uncertainties or ranges of the reported data [39–44]. The error bars associated with the uncertainty in r reflect, we believe, the fact that the importance of the lattice parameters was not recognized and so was not measured with high precision. The results in Fig. 5b are consistent with the major trend that increasing r increases the ductility and hence toughness per unit volume of austenite. Two dominant alloying trends emerge as favorable in these particular alloys: increasing C content, which resides mainly in the FCC γ phase and increases a_{fcc} with minimal changes to a_{bcc} [45], and increasing Si content, which decreases a_{bcc} with minimal changes to a_{fcc} [46,47]. Note, that due to small austenite grain sizes of the low-alloyed steels in Fig. 5, the C contents do not induce tetragonality of the fresh martensite up to ~ 1.5wt% [45]. The alloys with the largest austenite carbon contents $\mathbf{C}_\gamma$ are associated with the large error bars, that might be also due to the occurrence of tetragonal/twinned martensite for some of the alloys, or to the occurrence of lenticular martensite [48]. The significant scatter in the data precludes high quantification, but supports the general trend. Additional scatter enters because other factors such as precise microstructure and yield strength can enter into the determination of the elongation, and controlling the evolution of the transformation is also important [12]. Nonetheless, the important relationship between mechanical performance and lattice parameter ratio r is suitably supported.

6. Conclusions

To conclude, in the present investigation we were able to monitor *in-situ* the growth of lath martensite in a Fe-20.2Ni-5.4Mn (wt.%) alloy. The in-plane strain components recorded by HR-DIC were further interpreted using a recent crystallographic theory of martensite. The experiment/theory synergy yields for the first time an accurate measurement of the *in-situ* transformation strain in this alloy, which is ~ 40%.

With the new understanding of the importance of r revealed by theory now validated against experiments, future alloy design of composition and thermo-mechanical processing can be pursued by controlling r as well as controlling the established and still crucial quantities of FCC/BCC transformation temperature and FCC volume fraction. However, control of r might be achieved by many different possible alloying elements at low concentrations (not solely the C and Si relevant in the experiments shown in Fig. 5b), enabling higher ductility even in systems that have lower austenite content, for example. Such a design strategy can, furthermore, be guided by *ab-initio* computations, which can assess both FCC-BCC thermodynamics and changes in lattice parameters (and therefore lattice parameter ratio) as a function of alloying. Such guided design should enable accelerated discovery of new steels with high toughness.

Contributions

All authors designed the research. E.P. and M.S. performed the experiments. F.M. performed the modeling. All authors analyzed the data, discussed the results, and wrote the paper.

Declaration of Competing Interest

The authors declare that they do not have any financial or non-financial conflict of interests.

Acknowledgments

Support for this work was provided through the European Research Council Advanced Grant “Predictive Computational Metallurgy”, ERC Grant agreement No. 339081 - PreCoMet, and through the European Research Council Advanced Grant “Multiaxial and Multiscale Plasticity in Metals”, ERC Grant agreement No. 339245 - MULTIAX. Computational resources were supported by EFPL funding to the LAMMM lab and executed through the EPFL SCITAS HPC facility. The authors acknowledge Mr. A. Weible and Mr. T. Meisner (Max Planck Institute for Intelligent Systems, Germany) for the material preparation, Dr. Annick Baur (EPFL, Switzerland) for the heat treatment to induce thermal martensite, Dr. Jan Capek (PSI, Switzerland) for performing the neutron diffraction experiments at POLDI, SINQ, Mr. Wei-Neng Hsu (PSI and EPFL, Switzerland), Dr. Rolf Brönnimann (EMPA, Switzerland) for the sample preparation with the picosecond laser, and Dr. Michal Jambor (IPM CAS, Czech Republic) for acquiring SAED for lattice parameter measurements. The authors would like to acknowledge the anonymous reviewer, whose remarks contributed to improving the paper in the present form.

Appendix A. Application of Crystallographic Theory using Experimental Input

For the Fe-20.2Ni-5.4Mn alloy studied here, the lattice parameter ratio is measured with TEM and neutron diffraction to be $a_{\text{fcc}}/a_{\text{bcc}} = 1.233$, and the average orientation relationship $\varphi = 3.7^\circ$ is taken based on HRTEM measurements [20]. The determination of $\mathbf{P}^{(1)}$ is done here by considering experimental austenite crystal coordinates and the *in-situ* measurement of crystallographic martensite variants (relative orientation of martensite with respect to austenite).

A1. Identification of the single phase orientation from EBSD measurements

We analyze the austenite orientations around martensite island labeled as 1 in Fig. 1. We measure the Martensite 1 Euler angles as well as a distribution (5 points) of austenite Euler angles all around it. Error bars relative to strain predictions (Fig. 2) show that such

Table 1
Martensite 1 orientation and distribution of Austenite orientations.

Site	α	β	γ	$\Delta\zeta_{ij}$
Martensite 1	97.5	133.1	9.7	–
Austenite 1	266.8	90.3	270.7	–
Austenite 2	266.7	90.3	271.8	1.1051
Austenite 3	267.8	91.0	0.2	1.3234
Austenite 4	89.0	88.9	358.0	2.6645
Austenite 5	266.9	89.9	271.4	0.8123

distribution barely affects the strain magnitude. The Euler angles convention adopted by the OIM software [34] is the Bunge's passive convention [35]. Euler angles are provided in degrees and we indicate them as α, β and γ in Supplementary Table 1. Passive convention means that the matrix performs a change from global to crystal coordinates. Since we are interested in the inverse transformation, we take the transpose of this matrix to change from crystal to global coordinates.

Austenite orientations in the different measurement points are equivalent by axis relabeling/reflections. We indicate with $\Delta\zeta_{ij}$ the actual orientation fluctuations within the austenite, which are computed (see below) as a function of Austenite orientation 1. These fluctuations compare with EBSD measurement accuracy (~ 2°) and do not influence visibly predictions (Fig. 2).

To determine the magnitude of above fluctations, we first write the rotation matrices $\mathbf{R}_{Ai}$ related to the ith austenite measurements of the triplet (α_i, β_i, γ_i). One of such matrices reads

$$\mathbf{R}_{Ai} = \begin{pmatrix} \cos(\gamma_i)\cos(\alpha_i) - \sin(\gamma_i)\cos(\beta_i)\sin(\alpha_i) & \cos(\gamma_i)\sin(\alpha_i) + \sin(\gamma_i)\cos(\beta_i)\cos(\alpha_i) & \sin(\gamma_i)\sin(\beta_i) \\ -\sin(\gamma_i)\cos(\alpha_i) - \cos(\gamma_i)\cos(\beta_i)\sin(\alpha_i) & -\sin(\gamma_i)\sin(\alpha_i) + \cos(\gamma_i)\cos(\beta_i)\cos(\alpha_i) & \cos(\gamma_i)\sin(\beta_i) \\ \sin(\beta_i)\sin(\alpha_i) & -\sin(\beta_i)\cos(\alpha_i) & \cos(\beta_i) \end{pmatrix}^T \tag{5}$$

We write the misorientation of austenite with respect to $\mathbf{R}_{A1}$, namely the rotation matrix related to Austenite 1. A misorientation between matrix i and j is given by

$$\mathbf{R}_{\Delta ij} = \mathbf{R}_{Ai} \cdot \mathbf{R}_{Aj}^T \tag{6}$$

where ^{T} indicates transposition.

If the matrices differ by a simple rotation, then the eigenvector related to the only real eigenvalue of the matrix is the rotation axis **c**. The amount of rotation (misorientation) $\Delta\zeta_{ij}$ is obtained by computing

$$\Delta\zeta_{ij} = \cos^{-1}\left[\mathbf{b}\cdot\left(\mathbf{R}_{\Delta ij}\cdot\mathbf{b}\right)\right] \tag{7}$$

where **b** is any unimodular vector perpendicular to the rotation axis, which can be computed by taking any vector **a** not parallel to the axis **c**

$$\mathbf{b} = \frac{\mathbf{a}\times\mathbf{c}}{\|\mathbf{a}\times\mathbf{c}\|}. \tag{8}$$

If the matrices i and j differ also by a reflection, this must be first obtained before the misorientation is calculated. We obtained these reflections $\mathbf{R}_{Rij}$ by inspection, yielding the misorientation

$$\mathbf{R}_{\Delta ij} = \mathbf{R}_{Ai}\cdot\left(\mathbf{R}_{Rij}\cdot\mathbf{R}_{Aj}\right)^T. \tag{9}$$

All misorientation angles $\Delta\zeta_{ij}$ calculated with the above procedure are listed in Table 1 with respect to Austenite 1. Finally, also the martensite island rotation matrix $\mathbf{R}_M$ is determined according to Eq. (5).

Table 2
Measured orientation relationships for Martensite 1. A-# indicates the number of the Austenite measurement.

Site	Parallel plane	Parallel direction	$d\theta$ (°)	$d\xi$ (°)
A-1 / M	$(11\bar{1})_{fcc}\|(\bar{1}01)_{bcc}$	$[\bar{1}0\bar{1}]_{fcc}\|[010]_{bcc}$	1.7713	2.9234
A-2 / M	$(11\bar{1})_{fcc}\|(\bar{1}01)_{bcc}$	$[\bar{1}0\bar{1}]_{fcc}\|[010]_{bcc}$	1.591	3.6129
A-3 / M	$(\bar{1}11)_{fcc}\|(10\bar{1})_{bcc}$	$[01\bar{1}]_{fcc}\|[010]_{bcc}$	3.088	3.1588
A-4 / M	$(11\bar{1})_{fcc}\|(10\bar{1})_{bcc}$	$[011]_{fcc}\|[010]_{bcc}$	3.7927	5.2615
A-5 / M	$(11\bar{1})_{fcc}\|(\bar{1}01)_{bcc}$	$[\bar{1}0\bar{1}]_{fcc}\|[010]_{bcc}$	1.4667	3.585

A2. Identification of the martensite variants

We now determine the orientation relationships according to measurements. The orientation relationship brings a vector or a plane normal in the austenite (A) reference into the martensite (M) frame according to

$$\mathbf{R}_{A\to M} = \mathbf{R}_M^T \cdot \mathbf{R}_A. \tag{10}$$

For each austenite measurement, we need to identify the close-packed fcc and bcc planes that are closest to be parallel, and the close-packed fcc directions parallel to $\langle 100\rangle_{bcc}$, which determines the Bain group [17]. The crystallographic plane is found by applying the transformation $\mathbf{R}_{A\to M}$ to all possible planes in a fcc lattice, and by checking which one is the closest to being unrotated. The crystallographic direction is obtained by finding the austenite close-packed direction which is contained in the close-packed plane and is closest to a $\langle 100\rangle_{bcc}$ direction. Results for all variants are shown in Table 2. Misorientations $d\theta$ and $d\xi$ indicate deviations from perfect parallelism of planes and directions.

We then define as master the Nishiyama-Wassermann (NW) orientation relationship, with respect to which we calculate $\mathbf{P}^{(1)}$,

$$\begin{matrix} (111)_{A_M} & \| (011)_{M_M} \\ [1\bar{1}0]_{A_M} & \| [100]_{M_M} \end{matrix} \tag{11}$$

For any angle $\varphi \neq 5.26°$, there are in general two variants associated with the master orientation relationship (11). The typical misorientation of these two variants for $\varphi = 3.7°$ is ~ 3.12° and thus it is close to EBSD measurement resolution and it is difficult to be accurately assessed. We thus calculate $\mathbf{P}^{(1)}$ for both variants. It turns out that one of the two variants is associated with a shape deformation which is totally unrelated to experimental measurements (both in terms of strain signs and magnitudes) and hence this solution is ruled out.

It is necessary to convert the result for the master variant to the specific variant identified experimentally. This is achieved by inspection following three steps. In the first step, the corresponding bcc planes and directions listed in Table 2 are identified and rewritten in the austenite lattice having orientation A' associated with the Bain group of the master variant. In the second step, the transformation $\mathbf{T}_{A_M\to A'}$ is determined between master planes and directions and the A' planes and directions. Note, that if experimental martensite planes and directions coincide with those identifying the master variant A', such operation is an identity. In the third step, the transformation $\mathbf{T}_{A'\to A}$ is determined between the austenite planes and directions in orientation A' and the experimental austenite planes and directions in Table 2.

The conversion from master to experimental variant is then achieved by the transformation $\mathbf{T}_{A_M\to A} = \mathbf{T}_{A_M\to A'}\cdot\mathbf{T}_{A'\to A}$.

Table 3 reports the transformation matrices associated with all measured orientations.

Table 3
Transformation matrices $\mathbf{T}_{A_M \to A}$.

Site	$\mathbf{T}_{A_M \to A}$
A1 / M	$\begin{pmatrix} 0 & 1 & 0 \\ 0 & 0 & 1 \\ -1 & 0 & 0 \end{pmatrix}$
A2 / M	$\begin{pmatrix} 0 & 1 & 0 \\ 0 & 0 & 1 \\ -1 & 0 & 0 \end{pmatrix}$
A3 / M	$\begin{pmatrix} 0 & 0 & -1 \\ 1 & 0 & 0 \\ 0 & 1 & 0 \end{pmatrix}$
A4 / M	$\begin{pmatrix} 0 & 0 & 1 \\ 1 & 0 & 0 \\ 0 & -1 & 0 \end{pmatrix}$
A5 / M	$\begin{pmatrix} 0 & 1 & 0 \\ 0 & 0 & 1 \\ -1 & 0 & 0 \end{pmatrix}$

A3. Prediction of the in-situ *transformation strain, using experimental input*

Once the transformation matrices are determined, the shape deformation $\mathbf{P}^{(1)*}$ written in the specimen reference is

$$\mathbf{P}^{(1)*} = \mathbf{R}_A \cdot \mathbf{T}_{A_M \to A} \cdot \mathbf{P}^{(1)} \cdot \mathbf{T}^T_{A_M \to A} \cdot \mathbf{R}^T_A \tag{12}$$

DIC measurements of strain are provided in terms of three in-plane components of the Green-Lagrange strain, which are measured according to (see Ncorr manual [31])

$$\begin{aligned} E_{xx} &= \frac{1}{2}\left[2\frac{\partial u}{\partial x} + \left(\frac{\partial u}{\partial x}\right)^2 + \left(\frac{\partial v}{\partial x}\right)^2\right] \\ E_{xy} &= \frac{1}{2}\left[\frac{\partial u}{\partial y} + \frac{\partial v}{\partial x} + \frac{\partial u}{\partial x}\frac{\partial u}{\partial y} + \frac{\partial v}{\partial x}\frac{\partial v}{\partial y}\right] \\ E_{yy} &= \frac{1}{2}\left[2\frac{\partial v}{\partial y} + \left(\frac{\partial u}{\partial y}\right)^2 + \left(\frac{\partial v}{\partial y}\right)^2\right] \end{aligned} \tag{13}$$

In equations above, u and v are the displacements along the x and y directions, respectively. We use the same quantities as Eq. (13) for predictions, by calculating

$$\nabla \mathbf{u} = \mathbf{P}^{(1)*} - \mathbf{I} \tag{14}$$

where $\nabla \mathbf{u} = \left(\frac{\partial u}{\partial x}, \frac{\partial v}{\partial y}, \frac{\partial w}{\partial z}\right)$. Then the strain components (13) are calculated by substituting the relevant components of $\nabla \mathbf{u}$.

Table 4
Average and standard deviation of the in-plane strain component measurements, in the regions A, B, C, D, and E where transformation occurs (see Fig. 6).

Region	E_{xx}	E_{yy}	E_{xy}
A	−0.0917 (±0.0128)	0.1495 (±0.0164)	0.0234 (±0.0099)
B	−0.0784 (±0.0117)	0.1522 (±0.0152)	0.0103 (±0.0112)
C	−0.0735 (±0.0134)	0.1434 (±0.0158)	−0.0237 (±0.0099)
D	−0.0685 (±0.0212)	0.1338 (±0.0241)	0.02531 (±0.0118)
E	−0.0348 (±0.0133)	0.1288 (±0.0193)	−0.0064 (±0.0112)

Table 5
Average and standard deviation of the in-plane strain component measurements, in the regions A, B, C (highlighted in Fig. 6) and F (see Fig. 7).

Region	E_{xx}	E_{yy}	E_{xy}
A	−0.1091 (±0.0197)	0.187 (±0.0221)	0.0138 (±0.0104)
B	−0.1261 (±0.0183)	0.2373 (±0.0288)	0.0055 (±0.0121)
C	−0.1024 (±0.0247)	0.2003 (±0.0245)	0.0294 (±0.0141)
F	−0.1073 (±0.018)	0.2138 (±0.0384)	0.0169 (±0.0184)

Appendix B. HR-DIC measurement of in-plane strains

Fig. 6 shows the HR-DIC maps of the three in-plane strain components, E_{xx}, E_{xy} and E_{zz}, measured at 5.2% global strain.

The average and standard deviation of the measured in-plane strain components in these regions are reported in the Table 4.

Fig. 7 shows the HR-DIC maps of the three in-plane strain components, E_{xx}, E_{xy} and E_{zz}, measured at 7.7% global strain (and using as reference 0%). The region F is highlighted, where new martensite has formed.

The average and standard deviation of the measured in-plane strain components in these regions are reported in the Table 5.

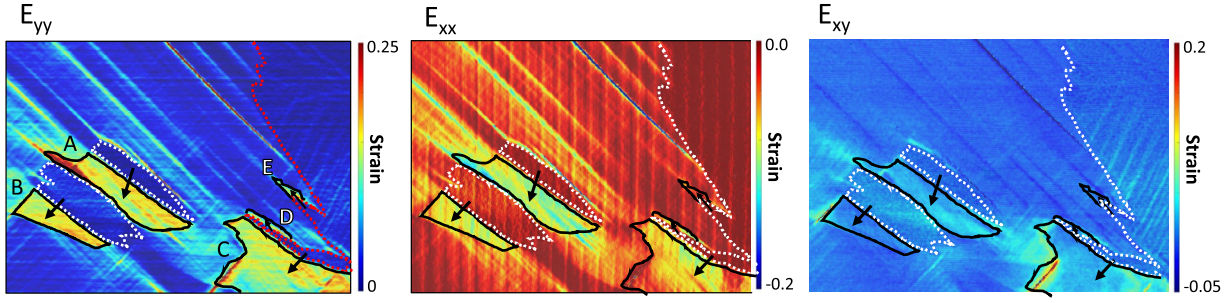

Fig. 6. HR-DIC measurements of austenite-martensite phase transformation. HR-DIC maps showing the growth of the martensite islands (indicated with black arrows) at 5.2% global strain (415 MPa) for the E_{yy}, E_{xx} and E_{xy} strain components.

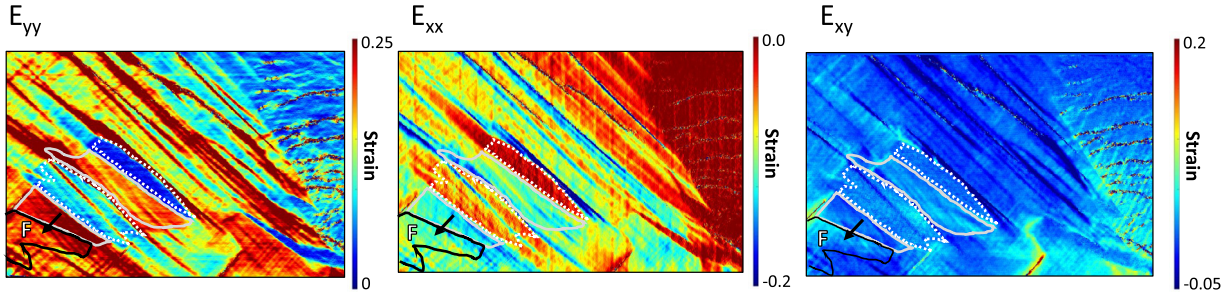

Fig. 7. HR-DIC measurements of austenite-martensite phase transformation. HR-DIC maps showing the growth (indicated with the black arrow) of the martensite island F at 7.7% global strain (435 MPa) for the E_{yy}, E_{xx} and E_{xy} strain components.

References

[1] M. Koyama, Z. Zhang, M. Wang, D. Ponge, D. Raabe, K. Tsuzaki, H. Noguchi, C.C. Tasan, Bone-like crack resistance in hierarchical metastable nanolaminate steels, Science 355 (2017) 1055–1057.

[2] G. Krauss, A.R. Marder, The morphology of martensite in iron alloys, Metall. Trans. 2 (1971) 2343–2357.

[3] S. Morito, H. Tanaka, R. Konishi, T. Furuhara, T. Maki, The morphology and crystallography of lath martensite in Fe-C alloys, Acta Mater. 51 (2003) 1789–1799.

[4] S. Morito, X. Huang, T. Furuhara, T. Maki, N. Hansen, The morphology and crystallography of lath martensite in alloy steels, Acta Mater. 54 (2006) 5323–5331.

[5] E. De Moor, S. Lacroix, A. Clarke, J. Penning, J.G. Speer, Effect of retained austenite stabilized via quench and partitioning on the strain hardening of martensitic steels, Metall. Mater. Trans. A 39 (2008) 2586–2595.

[6] D. Raabe, S. Sandlöbes, J. Millán, D. Ponge, H. Assadi, M. Herbig, P.P. Choi, Segregation engineering enables nanoscale martensite to austenite phase transformation at grain boundaries: a pathway to ductile martensite, Acta Mater. 61 (2013) 6132–6152.

[7] M.-M. Wang, C.C. Tasan, D. Ponge, A. Kotska, D. Raabe, Smaller is less stable: Size effects on twinning vs. transformation of reverted austenite in TRIP–maraging steels, Acta Mater. 79 (2014) 268–281.

[8] B.P.J. Sandvik, C.M. Wayman, Characteristics of lath martensite: part iii. Some theoretical considerations, Metall. Mater. Trans. A 14 (1983) 835–844.

[9] H.K.D.K. Bhadeshia, C.M. Wayman, Phase transformations: nondiffusive, In Physical Metallurgy, fifth ed., Elsevier, 2014.

[10] F. Roters, P. Eisenlohr, L. Hantcherli, D.D. Tjahjanto, T.R. Bieler, D. Raabe, Overview of constitutive laws, kinematics, homogenization and multiscale methods in crystal plasticity finite-element modeling: theory, experiments, applications, Acta Mater. 58 (2010) 1152–1211.

[11] P.J. Jacques, J. Ladriére, F. Delannay, On the influence of interactions between phases on the mechanical stability of retained austenite in transformation-induced plasticity multiphase steels, Metall. Mater. Trans. A 32 (2001) 2759–2768.

[12] M.-M. Wang, C.C. Tasan, D. Ponge, D. Raabe, Spectral TRIP enables ductile 1.1 GPa martensite, Acta Mater. 111 (2016) 262–272.

[13] F. Marketz, F.D. Fischer, Micromechanical modelling of stress-assisted martensitic transformation, Modell. Simul. Mater. Sci. Eng. 2 (1994) 1017.

[14] M. Cherkaoui, M. Berveiller, X. Lemoine, Couplings between plasticity and martensitic phase transformation: overall behavior of polycrystalline TRIP steels, Int. J. Plast. 16 (2000) 1215–1241.

[15] S. Turteltaub, A.S.J. Suiker, Grain size effects in multiphase steels assisted by transformation-induced plasticity, Int. J. Solids Struct. 43 (2006) 7322–7336.

[16] V.G. Kouznetsova, M.G.D. Geers, A multi-scale model of martensitic transformation plasticity, Mech. Mater. 40 (2008) 641–657.

[17] F. Maresca, V.G. Kouznetsova, M.G.D. Geers, W.A. Curtin, Contribution of austenite-martensite transformation to deformability of advanced high strength steels: from atomistic mechanisms to microstructural response, Acta Mater. 156 (2018) 463–478.

[18] B.P.J. Sandvik, C.M. Wayman, Crystallography and substructure of lath martensite formed in carbon steels, Metallography 16 (1983) 199–227.

[19] B.P.J. Sandvik, C.M. Wayman, Characteristics of lath martensite: part i. Crystallographic and substructural features, Metall. Mater. Trans. A 14 (1983) 809–822.

[20] T. Moritani, N. Miyajima, T. Furuhara, T. Maki, Comparison of interphase boundary structure between bainite and martensite in steel, Scr. Mater. 47 (2002) 193–199.

[21] K. Ogawa, S. Kajiwara, High-resolution electron microscopy study of ledge structures and transition lattices at the austenite–martensite interface in fe-based alloys, Phil. Mag. 84 (2004) 2919–2947.

[22] G. Miyamoto, A. Shibata, T. Maki, T. Furuhara, Precise measurement of strain accommodation in austenite matrix surrounding martensite in ferrous alloys by electron backscatter diffraction analysis, Acta Mater. 57 (2009) 1120–1131.

[23] F.D. Gioacchino, J.Q.d. Fonseca, Plastic strain mapping with sub-micron resolution using digital image correlation, Exp. Mech. 53 (2013) 743–754.

[24] F. Maresca, W.A. Curtin, The austenite/lath martensite interface in steels: Structure, athermal motion, and in-situ transformation strain revealed by simulation and theory, Acta Mater. 134 (2017) 302–323.

[25] K. Bhattacharya, Microstructure of Martensite: Why It Forms and How It Gives Rise to the Shape-Memory Effect, Oxford University Press, 2003.

[26] U. Stuhr, H. Spitzer, J. Egger, A. Hofer, P. Rasmussen, D. Graf, A. Bollhalder, M. Schild, G. Bauer, W. Wagner, Time-of-flight diffraction with multiple frame overlap part ii: the strain scanner POLDI at PSI, Nucl. Instrum. Meth. A 545 (2005) 330–338.

[27] U. Stuhr, M. Grosse, W. Wagner, The TOF-strain scanner POLDI with multiple frame overlap–concept and performance, Mater. Sci. Eng A 437 (2006) 134–138.

[28] O. Arnold, J.C. Bilheux, J.M. Borreguero, A. Buts, S.I. Campbell, L. Chapon, M. Doucet, N. Drapera, R.F. Leal, M.A. Gigga, V.E. Lynch, A. Markvardsen, D.J. Mikkelson, R.L. Mikkelson, R. Miller, K. Palmen, P. Parker, G. Passos, T.G. Perring, P.F. Peterson, S. Ren, M.A. Reuter, A.T. Savici, J.W. Taylor, R.J. Taylor, R. Tolchenov, W. Zhou, J. Zikovsky, Mantid-data analysis and visualization package for neutron scattering and μSR experiments, Nucl. Instr. Methods Phys. Res. A 764 (2014) 156–166.

[29] W.-N. Hsu, E. Polatidis, M. Šmid, S.V. Petegem, N. Casati, H.V. Swygenhoven, Deformation and degradation of superelastic NiTi under multiaxial loading, Acta Mater. 167 (2019) 149–158.

[30] S.V. Petegem, A. Guitton, M. Dupraz, A. Bollhalder, K. Sofinowski, M.V. Upadhyay, H.V. Swygenhoven, A miniaturized biaxial deformation rig for in situ mechanical testing, Exp. Mech. 57 (2017) 569–580.

[31] J. Blaber, B. Adair, A. Antoniou, Ncorr: open-source 2d digital image correlation MATLAB software, Exp. Mech. 55 (2015) 1105–1122.

[32] E.C. Bain, The nature of martensite, Trans. AIME 70 (1924) 25–47.

[33] B.P.J. Sandvik, C.M. Wayman, Characteristics of lath martensite: part ii. The martensite-austenite interface, Metall. Mater. Trans. A 14 (1983) 823–834.

[34] Orientation image microscopy (OIM) manual. Version 7.2, EDAX.

[35] H.J. Bunge, Texture analysis in materials science, mathematical methods (translated by P. R. Morris), Digital Edition, © Helga and Hans-Peter Bunge, Wolfratshausen, 2015.

[36] K. Wakasa, C.M. Wayman, The morphology and crystallography of ferrous lath martensite, Studies of Fe-20%Ni-%Mn–III. Surface relief, the shape strain and related features, Acta Metall. 29 (1981) 1013–1028.

[37] P.M. Kelly, Crystallography of lath martensite in steels, Mater. Trans. JIM 33 (1992) 235–242.

[38] L. Qi, J.W. Khachaturyan, J.W. Morris Jr., The microstructure of dislocated martensitic steel: theory, Acta Mater. 76 (2014) 23–39.

[39] S. Traint, A. Pichler, K. Hauzenberger, P. Stiaszny, E. Werner, Influence of silicon, aluminium, phosphorus and copper on the phase transformations of low alloyed TRIP–steels, Steel Res. 73 (2002) 259–266.

[40] W. Zhou, H. Guo, Z. Xie, X. Wang, C. Shang, High strength low-carbon alloyed steel with good ductility by combining the retained austenite and nano-sized precipitates, Mater. Sci. Eng. A 587 (2013) 365–371.

[41] J. Chiang, J.D. Boyd, A.K. Pilkey, Effect of microstructure on retained austenite stability and tensile behaviour in an aluminum-alloyed TRIP steel, Mater. Sci. Eng. A 638 (2015) 132–142.

[42] A. Grajcar, W. Kwaśny, W. Zalecki, Microstructure–property relationships in TRIP aided medium-c bainitic steel with lamellar retained austenite, Mater. Sci. Tech. 31 (2015) 781–794.

[43] D. Krizan, K. Spiradek-Hahn, A. Pichler, Relationship between microstructure and mechanical properties in nb-v microalloyed TRIP steel, Mater. Sci. Tech. 31 (2015) 661–668.

[44] A. Grajcar, A. Kilarski, A. Kozlowska, Microstructure-property relationships in thermomechanically processed medium-mn steels with high al content, Metals 8 (929) (2018) 1–19.

[45] E. Jimenez-Melero, N.H. van Dijk, L. Zhao, J. Sietsma, S.E. Offerman, J.P. Wright, S. van der Zwaag, Characterization of individual retained austenite grains and their stability in low-alloyed TRIP steels, Acta Mater. 55 (2007) 6713–6723.

[46] J. Zhang, F. Guyot, Thermal equation of state of iron and $Fe_{0.91}Si_{0.09}$, Phys. Chem. Minerals 26 (1999) 206–211.

[47] R. Blondé, E. Jimenez-Melero, L. Zhao, J.P. Wright, E. Brück, S. van der Zwaag, N.H. van Dijk, High-energy x-ray diffraction study on the temperature-dependent mechanical stability of retained austenite in low-alloyed TRIP steels, Acta Mater. 60 (2012) 565–577.

[48] M. Umemoto, E. Yoshitake, I. Tamura, The morphology of martensite in Fe–C, Fe–Ni–C And Fe–Cr–C alloys, J. Mater. Sci. 18 (1983) 2893–2904.

[49] P.M. Kelly, A. Jostsons, R.G. Blake, The orientation relationship between lath martensite and austenite in low carbon, low alloy steels, Acta Metall. Mater. 38 (1990) 1075–1081.